Deep-Sea Research II 123 (2016) 7–15

Contents lists available at ScienceDirect

Deep-Sea Research II

journal homepage: www.elsevier.com/locate/dsr2

Is the oceanic heat flux on the central Amundsen sea shelf caused by barotropic or baroclinic currents?

Ola Kalén [a,*], Karen M. Assmann [a], Anna K. Wåhlin [a], Ho Kyung Ha [b], Tae Wan Kim [c], Sang Hoon Lee [c]

[a] Department of Marine Sciences, University of Gothenburg, Sweden
[b] Inha University, Republic of Korea
[c] Korea Polar Research Institute, Republic of Korea

ARTICLE INFO

Available online 29 July 2015

Keywords:
Antarctica
Amundsen sea
Circulation
Ice shelf
Heat budget

ABSTRACT

The glaciers that drain the West Antarctic Ice Sheet into the Amundsen Sea are accelerating and experiencing increased basal melt of the floating ice shelves. Warm and salty deep water has been observed to flow southward in deep troughs leading from the shelf break to the inner shelf area where the glaciers terminate. It has been suggested that the melting induced by this warm water is responsible for the acceleration of the glaciers. Here we investigate the structure of the currents and the associated heat flow on the shelf using in-situ observations from 2008 to 2014 in Dotson Trough, the main channel in the western part of the Amundsen Sea shelf, together with output from a numerical model. The model is generally able to reproduce the observed velocities and temperatures in the trough, albeit with a thicker warm bottom layer. In the absence of measurements of sea surface height we define the barotropic component of the flow as the vertical average of the velocity. It is shown that the flow is dominated by warm barotropic inflows on the eastern side and colder and fresher barotropic outflows on the western side. The transport of heat appears to be primarily induced by this clockwise barotropic circulation in the trough, contrary to earlier studies emphasizing a bottom-intensified baroclinic inflow as the main contributor.

1. Introduction

The glaciers in the Amundsen Sea Embayment which drain the West Antarctic Ice Sheet have been losing mass at an increasing rate in recent decades (Pritchard et al., 2012; Rignot et al., 2014). There are indications that the major part of the ice sheet mass loss is due to thinning of the floating ice shelves (e.g. Paolo et al., 2015) induced by basal melting caused by warm salty ocean water that floods the continental shelf. The ice shelf cavities in the Amundsen Sea are accessed by relatively warm ($>0.5\,^{\circ}C$) and salty (>34.3 psu) deep water via submarine channels (Jacobs et al., 2011; Pritchard et al., 2012), and warm dense inflows have been observed on the Amundsen Sea shelf (Walker et al., 2007; Wåhlin et al., 2010, 2013; Jacobs et al., 2011; Assmann et al., 2013) as well as further east in Marguerite Trough, Bellingshausen Sea (Klinck et al., 2004; Moffat et al., 2009; Dinniman et al., 2011).

Processes thought to control the flow of warm deep water onto the shelf include an eastward undercurrent (Chavanne et al., 2010; Walker et al., 2013), bottom Ekman transport (Wåhlin et al., 2012), eddies (Thompson et al., 2014) and wind (Thoma et al., 2008; Wåhlin et al., 2013; Assmann et al., 2013). The inflow to the Pine Island, Thwaites and Crosson ice shelves in the east occurs through two outer troughs that merge into one, opening up into a deep subglacial basin close to the coast (Fig. 1). This trough is the deepest connection between the shelf break and the inner shelf basins in the Amundsen Sea Embayment. The main focus of this study is the trough further west, the Dotson trough, with a sill depth around 500 m, which channels the warm water towards Getz and Dotson ice shelves. The two troughs are separated by a 300–400 m shallow ridge leading up to Bear Peninsula (Fig. 1). Observations of the circulation pattern in both troughs show that warm water inflows are located on their eastern flanks (Walker et al., 2007; Wåhlin et al., 2010; Nakayama et al., 2013) and mooring data show that the inflows are present throughout the year (Arneborg et al., 2012; Wåhlin et al., 2013; Assmann et al., 2013; Ha et al., 2014). Colder and fresher meltwater-laden outflows have also been observed on the western flanks of the troughs (Ha et al., 2014;

* Corresponding author at: Department of Marine Sciences University of Gothenburg Box 460 40530 Gothenburg, Sweden. Tel.: +46 317862882.
E-mail address: ola.kalen@marine.gu.se (O. Kalén).

http://dx.doi.org/10.1016/j.dsr2.2015.07.014
0967-0645/

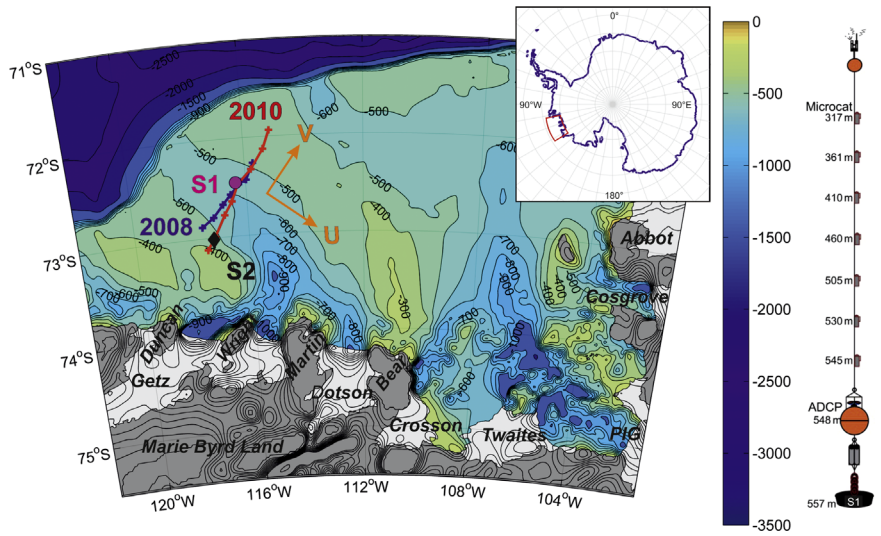

Fig. 1. Study area of Dotson trough on the Amundsen Sea shelf together with mooring setup. The blue and red lines are transects from the Oden expeditions of 2008 and 2010 respectively, with crosses showing the stations. The magenta circle is the mooring S1 and the black diamond is the mooring S2. The orange arrows show the rotation of the velocities to fit the orientation of the channel, with U as the along-trough velocity, positive towards southeast. Bathymetry from Timmermann et al. (2010). (For interpretation of the references to color in this figure legend, the reader is referred to the web version of this article.)

Nakayama et al., 2013; see also Herraiz-Borreguero et al. (2015) for western-flank outflows in Prydz Bay, East Antarctica).

The currents responsible for the heat flux towards the ice shelves were investigated by Arneborg et al. (2012) and Wåhlin et al. (2013) using data from a mooring on the eastern side of the Dotson trough equipped with current meters and temperature-salinity loggers measuring the bottom part of the water column. During the first 10 months of observations the average velocity was southward in the 150 m closest to the bottom, but northward in the water above the warm layer (Arneborg et al., 2012). However, extending the time series to 26 months revealed that the flow direction was southward at all depths (Wåhlin et al., 2013). The variability of the current was investigated using EOF analysis (Davis, 1976) and it was seen in both studies that the strongest mode of variability in velocity, responsible for about 90% of the variance, was nearly vertically constant, and that the second strongest mode was bottom intensified. The heat flux caused by the strongest mode of variability was small compared with the heat flux caused by the temporal average. Since the moored current meters only covered the 300 m closest to the bottom it was not possible to draw conclusions regarding the velocity structure higher in the water column from these data alone. The fact that the temporal average was positive at all depths for the 26 month record indicate that the barotropic currents may be stronger than the baroclinic, in contrast to what was observed in the first 10 months of measurements. Ship-borne Lowered Acoustic Doppler Current Profiler (LADCP) data covering the entire water column also indicate a strong barotropic velocity component (Wåhlin et al., 2010; Ha et al., 2014) with large spatial and temporal variability (Ha et al., 2014; Wåhlin et al., 2013).

Model studies with realistic (Schodlok et al., 2012) and idealized setups (St. Laurent et al., 2013) indicate that the vertically averaged current on the shelf flows in a clockwise pattern. However, these studies do not investigate the depth-varying structure of the circulation and the relative importance of its baroclinic and barotropic components. The aim of the present study is to investigate whether the ocean circulation responsible for bringing warm water southward onto the shelf and colder water northward out of the shelf, is barotropic or baroclinic in structure. To achieve this we use a combination of ship-borne and moored observations together with model data.

2. Data and methods

The data were collected during four austral summer cruises; *IB Oden* in 2008/09 and 2010/11 as well as *IB Araon* in early 2012 and 2013/2014. Both ships are equipped with Kongsberg EM122 12 kHz multi-beam echo-sounders for bottom profiling. The profiles for temperature, conductivity and depth used in this study were collected during the two Oden cruises with a Sea-Bird 911 plus CTD system. Currents were measured acoustically with an RDI Workhorse LADCP with 300 kHz frequency, which has approximately 150 m range. Fig. 1 shows the location of CTD/LADCP stations along two cross-trough transects. Two subsurface moorings were also deployed in the trough (Fig. 1), both equipped with an array of MicroCATs (SBE-37SMP) at 15–50 m intervals and an upward looking 150 kHz ADCP (RDI, QuarterMaster) that recorded vertical profiles of temperature, salinity, and velocity from the sea floor up to about 300 m. Mooring S1 (72.468°S, 116.358°W) on the eastern side of the trough was deployed in February 2010 and recovered in March 2012, while mooring S2 (73.016°S, 117.248°W) on the western flank was deployed in December 2010 and recovered in March 2012. All sensors were calibrated before and after the cruises and data corrected for drift in temperature and salinity. The velocity data from the moorings were detided with the T_tide harmonic analysis (Pawlowicz et al., 2002) and the LADCP data were detided with the Circumpolar Antarctic Tidal Simulation 2008 model (Padman et al., 2002).

The ocean model (Assmann et al., 2013) is a regional setup of MITgcm (Marshall et al., 1997), including a sea ice model (Losch et al., 2010) and a sub-ice shelf–ocean interaction scheme (Losch, 2008) on the domain 80°W–140°W and 76°S–62°S. The resolution is 0.1° longitude and $0.1° \times \cos(\varphi)$ latitude, corresponding to approximately 3.5 km in the channel, slightly less than the internal Rossby radius. The bathymetry and ice shelf draft used is RTOPO1.0.5 (Timmermann et al., 2010). The model contains 50 vertical levels, 20 of which are located in the upper 1000 m. The initial conditions were provided by World Ocean Atlas 2009 (WOA09) potential temperature (Locarnini et al., 2010) and salinity (Antonov et al., 2010) and the atmospheric forcing was the NCEP Climate Forecast System Reanalysis (CFSR) (Saha et al., 2010). For parameterization of the vertical mixing, the K-profile Parameterization (KPP) model (Large et al., 1994) was used. Salinity and potential temperature at the open boundaries were prescribed

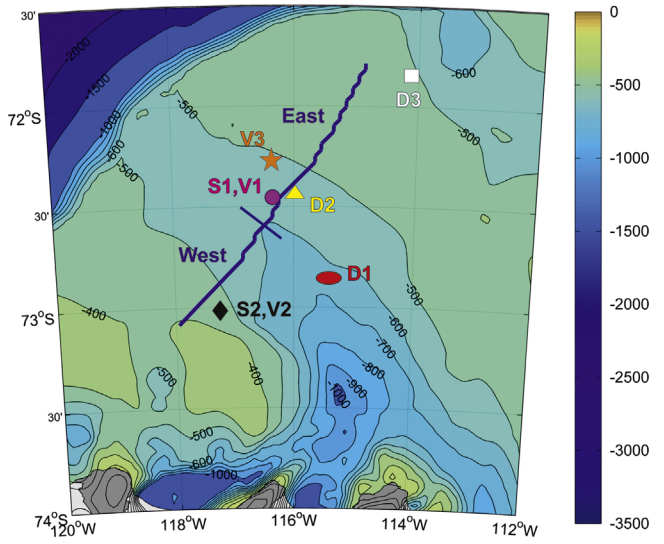

Fig. 2. Map of Dotson trough. The model transect (blue) approximately follows the two in-situ transects of the Oden expeditions (Fig. 1) and is divided into two parts, west and east, at the deepest position. The magenta circle is the position of the in-situ mooring S1 and the virtual mooring V1. The orange star is the position of the virtual mooring V3. The black diamond is the position of the mooring S2 and the virtual mooring V2. The red oval, the yellow triangle and the white square are the drift stations D1, D2 and D3 respectively. (For interpretation of the references to color in this figure legend, the reader is referred to the web version of this article.)

with monthly averages from WOA09. The boundary conditions for the velocities were assigned from a circumpolar setup of MITgcm with 0.25° resolution that was run with identical atmospheric forcing (Holland et al., 2014). The model was spun-up for 10 years using NCEP CFSR from the year 1980 as atmospheric forcing and then run from 1979 to 2011. The model does not include tides. Typical observed maximum tidal speeds range from 0.01 to 0.04 m s^{-1}, smaller than the vertical average velocities for most locations (Wåhlin et al., 2012). We used the model results for the years 1980–2011 for analysis and compared the last two years with the in-situ observations. For the comparison with the in-situ time series, three adjacent positions from the model were selected (V1–V3, see Fig. 2 for positions). The virtual moorings V1 and V2 use model data from the grid cells closest to the locations of the moorings S1 and S2, with a displacement of approximately 1 km from the real positions. However, since V1 was outside the main inflow core in the model, the more upslope position V3 approximately 19 km to the north was also studied.

To study the velocity components responsible for transporting oceanic heat on the shelf, a cross-trough section was identified in the model following the mean route of the two observed transects (Fig. 2). The section was split into a western and eastern part at the deepest point of the channel. The heat flux Q_H through the section is given by

$$Q_H = \int_{x_1}^{x_N} \int_{-D}^{-d} \rho C_p U (T - T_F) dz dx \quad (1)$$

where x is the horizontal coordinate (m) from grid point x_1 to x_N, $-D$ is the bottom depth (m), $-d$ is the level (m) up to which the integration is performed (the surface or the reach of the ADCP), ρ (kg m^{-3}) is the in-situ density, C_p (J K^{-1} kg^{-1}) is the specific heat capacity, dependent on the local temperature, salinity and pressure, U (m s^{-1}) is the along-trough velocity, T (K) is the temperature and T_F (K) is the temperature to which the water eventually cools, taken here to be the in-situ freezing temperature.

The in-situ velocities were divided into across-trough and along-trough directions (orange arrows, Fig. 1). The model velocities were similarly rotated for comparison to the mooring observations, but model fluxes were calculated based on the Arakawa C-grid (Arakawa and Lamb, 1977), with temperatures interpolated onto the velocity grid points to calculate heat transports.

The barotropic velocity is defined based on the gradient of sea surface height. However, since there are no observations of sea surface height available in this heavily sea ice covered area, the common approximation using the vertical average of the current was instead employed. The velocity U is hence decomposed into a barotropic (U_{BT}) and a baroclinic (U_{BC}) part,

$$U = U_{BT} + U_{BC} \quad (2)$$

where U_{BT} is defined as the vertical average velocity. A barotropic $Q_{H(BT)}$ and a baroclinic $Q_{H(BC)}$ heat transport is also defined based on (1) and (2),

$$Q_{H(BT)} = \int_{x_1}^{x_N} \int_{-D}^{-d} \rho C_p U_{BT} (T - T_F) dz dx \quad (3)$$

$$Q_{H(BC)} = \int_{x_1}^{x_N} \int_{-D}^{-d} \rho C_p U_{BC} (T - T_F) dz dx \quad (4)$$

3. Results

Fig. 3 shows the temporally averaged (2008–2011) velocity and temperature along the cross-trough transect in the model. In similarity with observations (Fig. 4; Arneborg et al., 2012; Wåhlin et al., 2013; Ha et al., 2014), the modeled warm layer is spread out leaning on the eastern side of the trough. A clockwise barotropic circulation is present in the trough, with south–eastward flow along the channel on the eastern flank and north–westward flow on the western flank which is also in line with observations, even though the simulated inflow is located further to the northeast (Fig. 4; Ha et al., 2014). The modeled velocities and temperatures on 22 Dec 2008 and 23 Dec 2010 agree qualitatively with the in-situ sections occupied those dates (Fig. 4). Finer scale structures are lacking in the model, indicating that the model resolution is too coarse to fully resolve all active processes (St. Laurent et al., 2013 and Assmann et al., 2013). Both

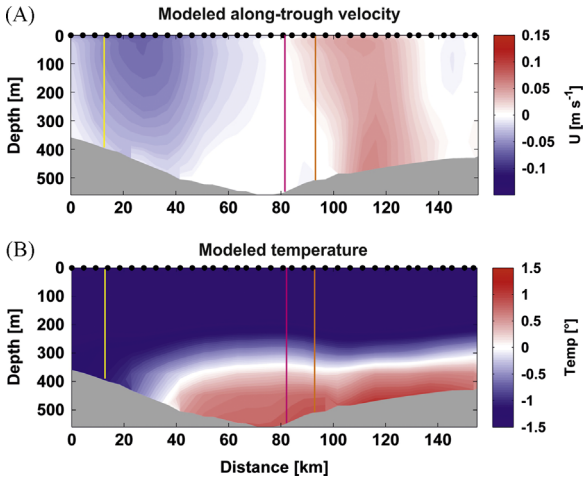

Fig. 3. Model data along the cross-trough section, with distance starting from southwest, temporal average from 2008 to 2011 of (a) along-trough velocity (m s^{-1}, positive towards southeast) and (b) temperature (°C). The black dots are the center of grid cells. The yellow and magenta lines show the approximate positions of moorings S2 and S1 respectively. The orange lines show the approximate position of the projection of the virtual mooring V3 onto the transect line. (For interpretation of the references to color in this figure legend, the reader is referred to the web version of this article.)

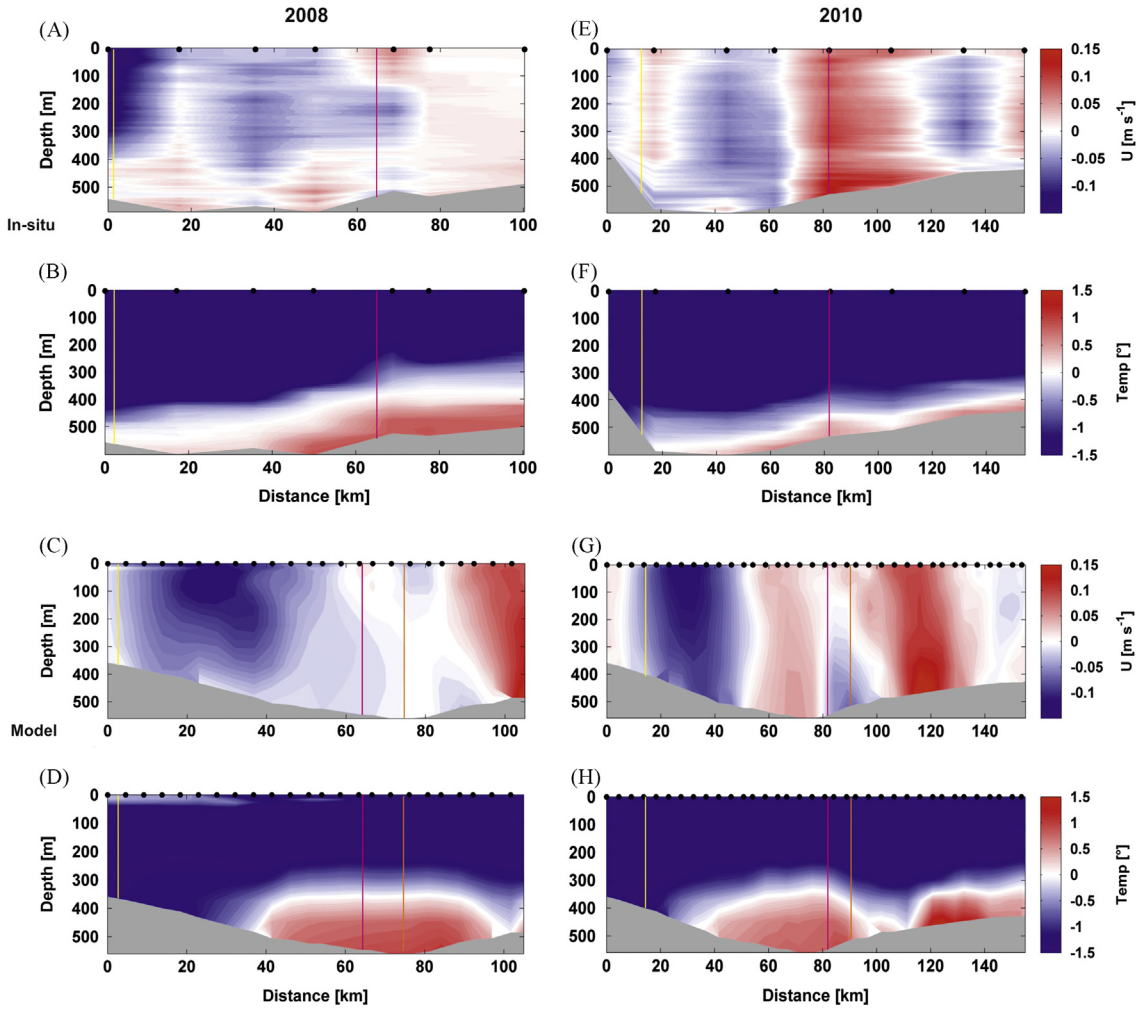

Fig. 4. Along-trough velocity (m s^{-1}, positive towards southeast) and temperature (°C) along the cross-trough sections, with distance starting from southwest. The yellow and magenta lines show the approximate positions of moorings S2 and S1 respectively. The orange lines show the approximate position of the projection of the virtual mooring V3 onto the transect line. (a) In situ along-trough velocity from 22 Dec 2008. The black dots are station positions, (b) In situ temperature from 22 Dec 2008, (c) Modeled along-trough velocity from 22 Dec 2008. The black dots are the center of grid cells, (d) Modeled temperature from 22 Dec 2008, (e) In situ along-trough velocity from 23 Dec 2010, (f) In situ temperature from 23 Dec 2010, (g) Modeled along-trough velocity from 23 Dec 2010 and (h) Modeled temperature from 23 Dec 2010. (For interpretation of the references to color in this figure legend, the reader is referred to the web version of this article.)

in-situ transects reveal inflows of warm water on the eastern slope of the trough (Fig. 4a and e). In the 2010 observations the inflowing warm layer was markedly colder and thinner than in 2008, while the simulated warm water layer was of approximately equal thickness and temperature in both years. The model reproduces the observed 2010 split of the warm layer into two warm cores east and west of 90 km along the section.

Figs. 5 and 6 show comparisons between the mooring and model data, illustrating the clockwise barotropic circulation observed and also recaptured in the model. On the eastern flank the mooring data (S1) is compared to two virtual mooring positions (V1 and V3). Position V3 was chosen to be closer to the modeled current core and velocities here are comparable with the observations (Fig. 5a and e) both in magnitude and variability, with periods of strong flow onto the shelf in July 2010, January–May 2011, and January 2012. However, since the model bathymetry is 64 m shallower than in reality, the temperature at V3 is lower and the variability in temperature larger than in the observations. Position V1, geographically closest to S1, is located outside the main simulated current core and thus the velocities are too low, but on the other hand the depth and temperatures are more similar to reality. For S2 (Fig. 6) the model bathymetry is 107 m too shallow, and modeled bottom temperatures are therefore colder than observations. There is qualitative agreement between the measured and modeled velocities on the western side, except for the lack of modeled inflows in the upper layers towards the end of the period.

In both model and observations warm water is continuously present in the bottom layer on the eastern slope (Fig. 5b, d and f) and shows a seasonally varying thickness (less pronounced in the model) with maximum in March–May. The warm layer is approximately 100 m thicker in the model than in observations, which also holds for the eastern Amundsen Shelf (Assmann et al., 2013). On the western flank, the temperature in the bottom layer is approximately 1.5 °C colder than on the eastern slope (Figs. 5 and 6), and fluctuates on daily time scales. There is generally a large discrepancy between the RTOPO1.0.5 bathymetry (Timmermann et al., 2010) used in the model and the multi-beam depth soundings from the Oden and the Araon expeditions (Fig. 7). In reality the trough is about 150 m deeper and its center is about 20 km further west compared with the RTOPO bathymetry (Fig. 7a). Close to the coast on the western side of the inland basin there are deep connections not represented in the RTOPO data (Fig. 7d).

The heat flux through the western and eastern part of the cross-trough section was calculated using (1). The total heat flux

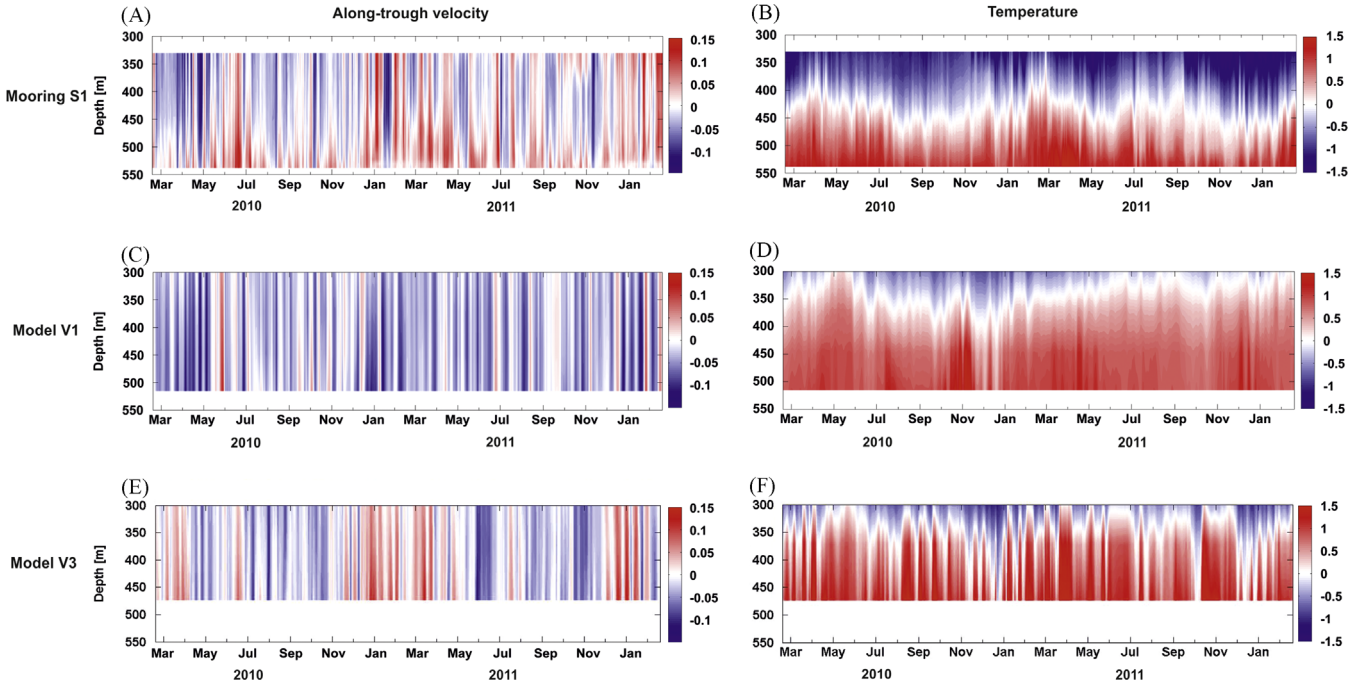

Fig. 5. Daily averages of along-trough velocity (m s^{-1}, positive towards southeast) and temperature (°C). (a) Observed along-trough velocity from mooring S1, (b) Observed temperature from mooring S1, (c) Modeled along-trough velocity from virtual mooring V1, (d) Modeled temperature from virtual mooring V1, (e) Modeled along-trough velocity from virtual mooring V3 and (f) Modeled temperature from virtual mooring V3.

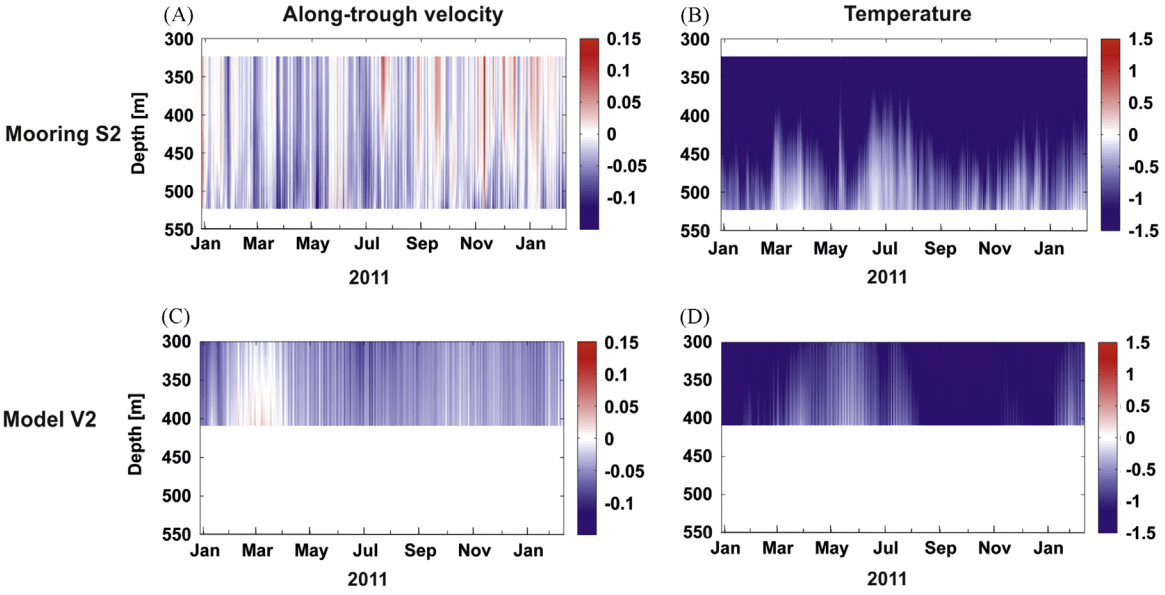

Fig. 6. Daily averages of along-trough velocity (m s^{-1}, positive towards southeast) and temperature (°C). (a) Observed along-trough velocity from mooring S2, (b) Observed temperature from mooring S2, (c) Modeled along-trough velocity from virtual mooring V2 and (d) Modeled temperature from virtual mooring V2.

was divided into a barotropic part (3) and a baroclinic part (4). The heat flux in the model was calculated using the integrals (3) and (4), including the variations in temperature and velocity over the virtual section (Fig. 2), but for the mooring data the horizontal integrals in (3) and (4) were approximated with an effective width, 80 km for S1 (Arneborg et al., 2012; Wåhlin et al., 2013) and 40 km for S2 (Ha et al., 2014). The observational data only contain the bottom part of the water column, while the model was integrated over the whole depth. However, since the upper 300 m of the in-situ temperatures are close to freezing point, the error on the total heat flux calculations is comparatively small and therefore results were similar when model data were only integrated over the lower part of the water column covered by the moorings (not shown). The outcome of the heat flux calculations are given in Fig. 8, showing the important result that the largest part of the heat flux is caused by the barotropic velocity, and the part of the heat flux that is induced by the baroclinic velocity is small in comparison. The temporal mean of the barotropic heat flux is positive on the eastern flank and negative on the western flank for both observations and model data. The mean values of the observational data, 3.25 TW on eastern side and −0.70 TW on the western side are similar to the values of Ha et al. (2014). The mean modeled heat fluxes give a weaker inflow of 2.10 TW, and a stronger outflow, −1.63 TW. Among possible explanations for the discrepancies between the model and observations on the eastern side is the shallow model bathymetry, while on the western side

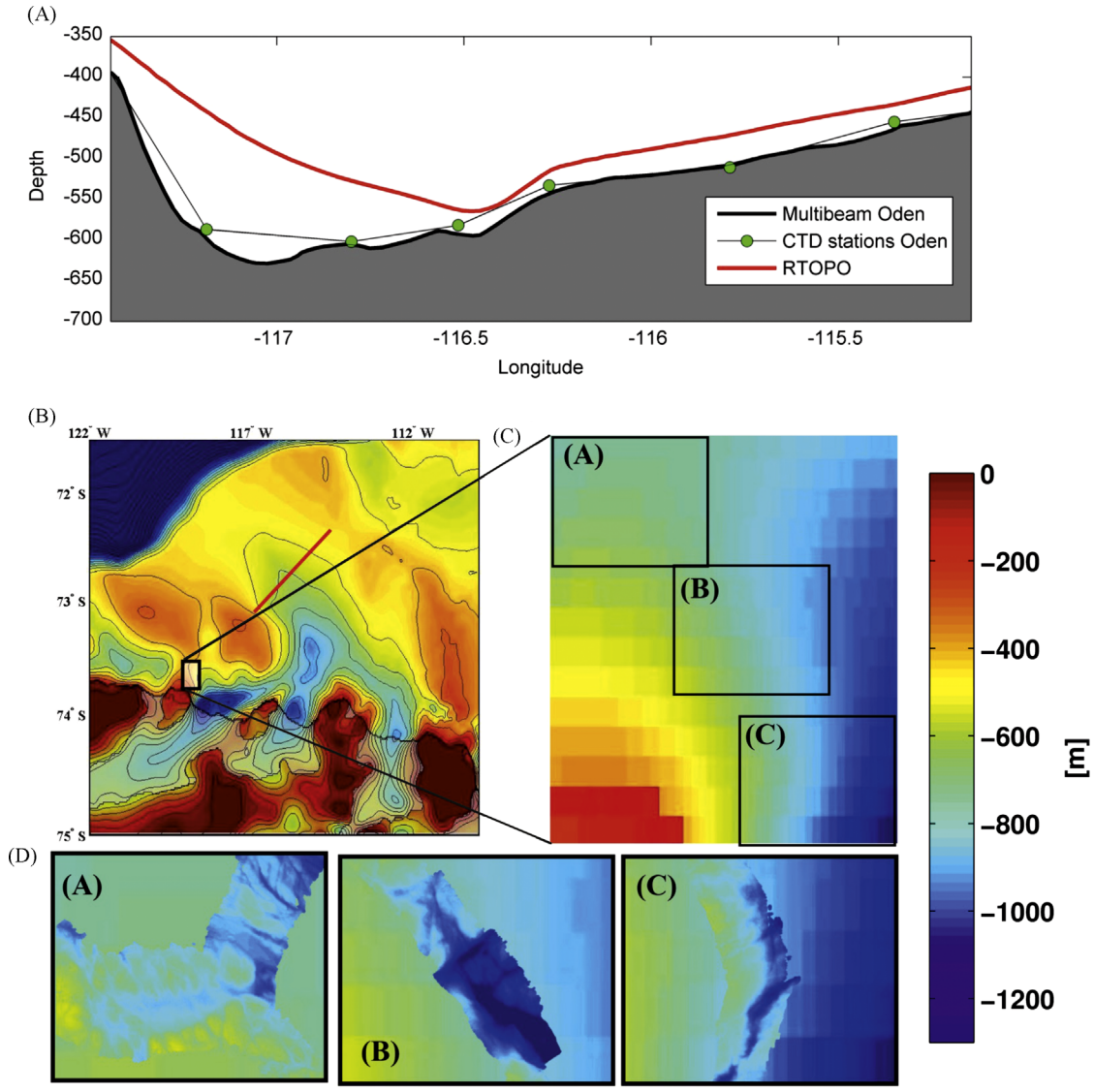

Fig. 7. Comparison between the RTOPO bathymetry (Timmermann et al., 2010) and multi-beam bathymetry obtained during the Oden cruise in 2010/2011 and the Araon cruise in 2013/2014. (a) Bathymetry across the section indicated by the red line in panel (b). Red line shows the RTOPO data, black line shows the multi-beam depth soundings from Oden 2010/2011, and green dots show the depth measured by the CTD altimeter. (b) RTOPO bathymetry data. (c) Focus area with the sub-panels (A), (B) and (C), indicated by the black rectangle in (b). (d) Multi-beam data from the Araon 2013/2014 cruise. The panels (A), (B) and (C) correspond to the areas in (c) showing the RTOPO data. (For interpretation of the references to color in this figure legend, the reader is referred to the web version of this article.)

the model lacks the periods of inflowing velocities found in the mooring (Fig. 6a and c). The effective width of 40 km used for the mooring data is also significantly shorter than the length of the model section on the western flank. The observed barotropic heat flux variability on the eastern side of the trough is distinctly larger than that in the model. The baroclinic heat flux generally gives a small positive contribution at both the eastern and western sides in both model and in situ data at most times, which is likely due to the geostrophic shear (compare e.g. Figs. 9 and 3).

Fig. 10 shows the modeled barotropic and baroclinic heat transports across the western and eastern parts of the cross-section for the period 1980–2011. The result that the barotropic circulation on the shelf is the main reason for the heat flux toward the glaciers is qualitatively similar to the two years for which comparisons have been made with the in situ data (Fig. 8), indicating that this finding is valid for the whole time period. The model results show periods of stronger barotropic circulation in the trough with higher variability, e.g. before 1990 and between 2002 and 2009, interspersed with calmer periods. This suggests that the time when the moorings were in the trough in 2010/11 was a period of relatively weak circulation and low variability.

Since the in situ data only covers the lower water column, a vertical average is not strictly representative for the whole water column. However, as noted by Arneborg et al. (2012) the largest mode of variability in the lower part of the water column is nearly depth independent, and it extends above the warm dense layer (Fig. 5) indicating that it could be barotropic. Depth-independent velocity components are strong in the cross-trough sections (Fig. 4a and e), where they extend above 300 m depth all the way to the surface. Fig. 11 shows the along-trough velocity and temperature measured during three drift stations (D1–D3, see Fig. 2 for positions) occupied by *IB Oden* in 2008/2009. In similarity with the cross-section velocities (Fig. 4) the drift stations show periods of depth-invariant flow extending above the warm layer supporting the assumption that the vertically averaged velocity observed in the moorings is representative for the whole water column, at least at times when it exceeds the baroclinic velocity. Periods of weak barotropic velocity, when the baroclinic velocity dominates, can also be noted (e.g. first half of station D1, Fig. 11a). Although snapshots in time, the transects and the drift stations support the findings from the moorings and model data

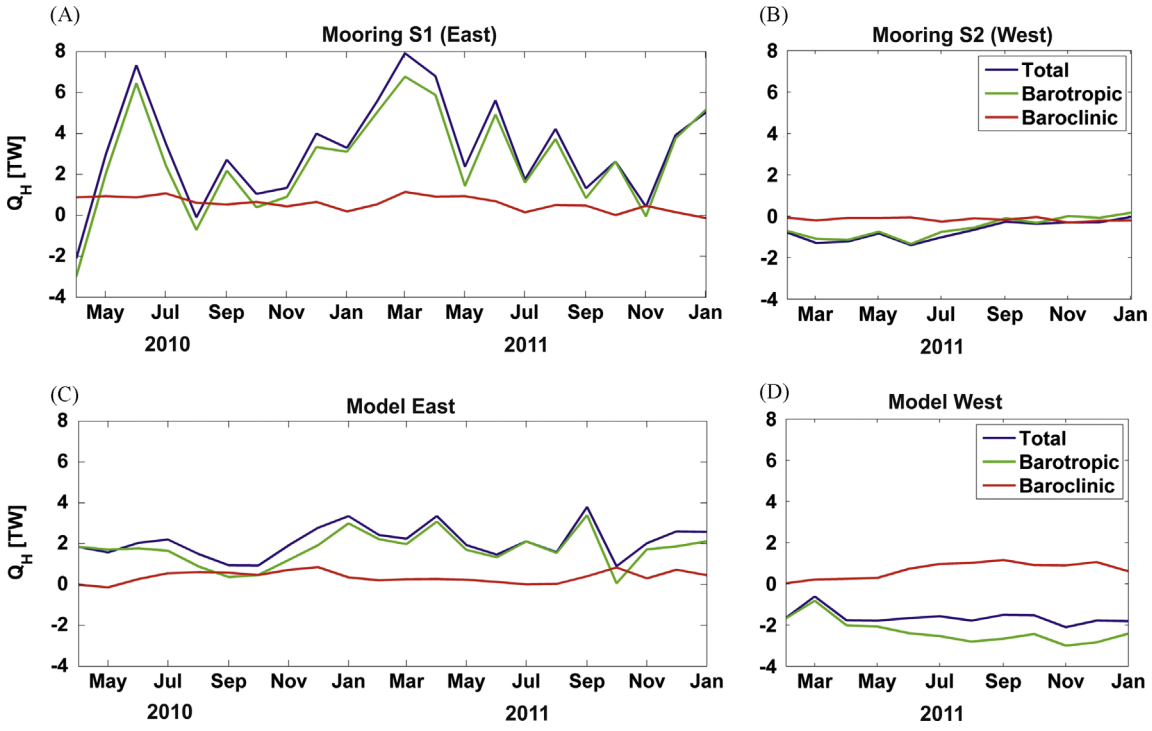

Fig. 8. Time series of monthly heat fluxes (TW) induced by the velocity components along the cross-trough sections. Times correspond to the deployment periods of the two moorings. (a) Eastern part, observational data, (b) Western part, observational data, (c) Eastern part, model data and (d) Western part, model data.

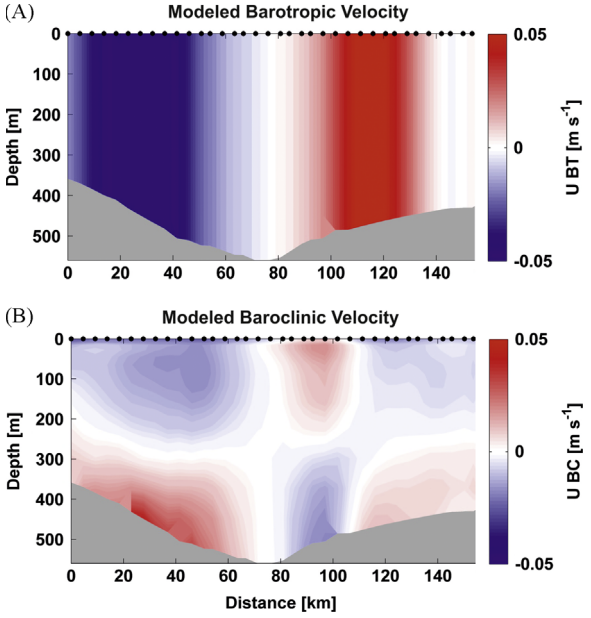

Fig. 9. Model data along the cross-trough section, with distance starting from southwest, temporal average from 1980 to 2011 of (a) along-trough barotropic velocity ($m\,s^{-1}$, positive towards southeast) and (b) along-trough baroclinic velocity. The black dots are the center of grid cells.

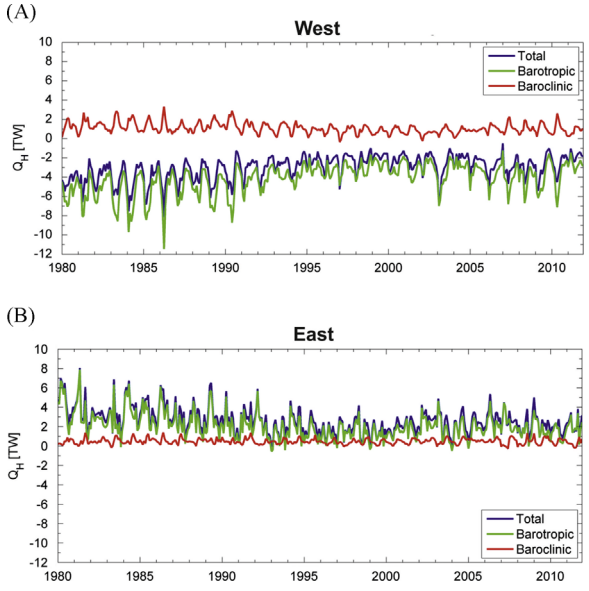

Fig. 10. (a) Monthly values of modeled heat flux (TW) induced by velocity components along the cross-trough transect, western part. Positive values directed towards southeast onto the shelf (b) Likewise as (a) but for eastern part.

that a barotropic velocity structure is often present and dominates the currents in the trough.

4. Discussion

The increase of basal melting under Getz Ice shelf between 2000 and 2007 was explained by Jacobs et al. (2013) to be caused by a thicker warm water layer occupying the shelf in the latter year. Our model time series places the colder, low basal melt year 2000 towards the end of a period of weak barotropic circulation in the trough and the warmer, high melt year 2007 in a period of strong barotropic heat fluxes (Fig. 10). The ability of the model to approximately reproduce these events strengthens our confidence in its utility for assessing ice shelf melt. Increased circulation was cited by Jacobs et al. (2011) as a mechanism to explain the rise in basal melt under Pine Island Glacier between 1994 and 2009. The results of our study indicate that a similar mechanism may also be at play further west, albeit in a more complex system, and that circulation strength as well as thermocline depth controls the access of warm deep water to the ice shelf bases in this area.

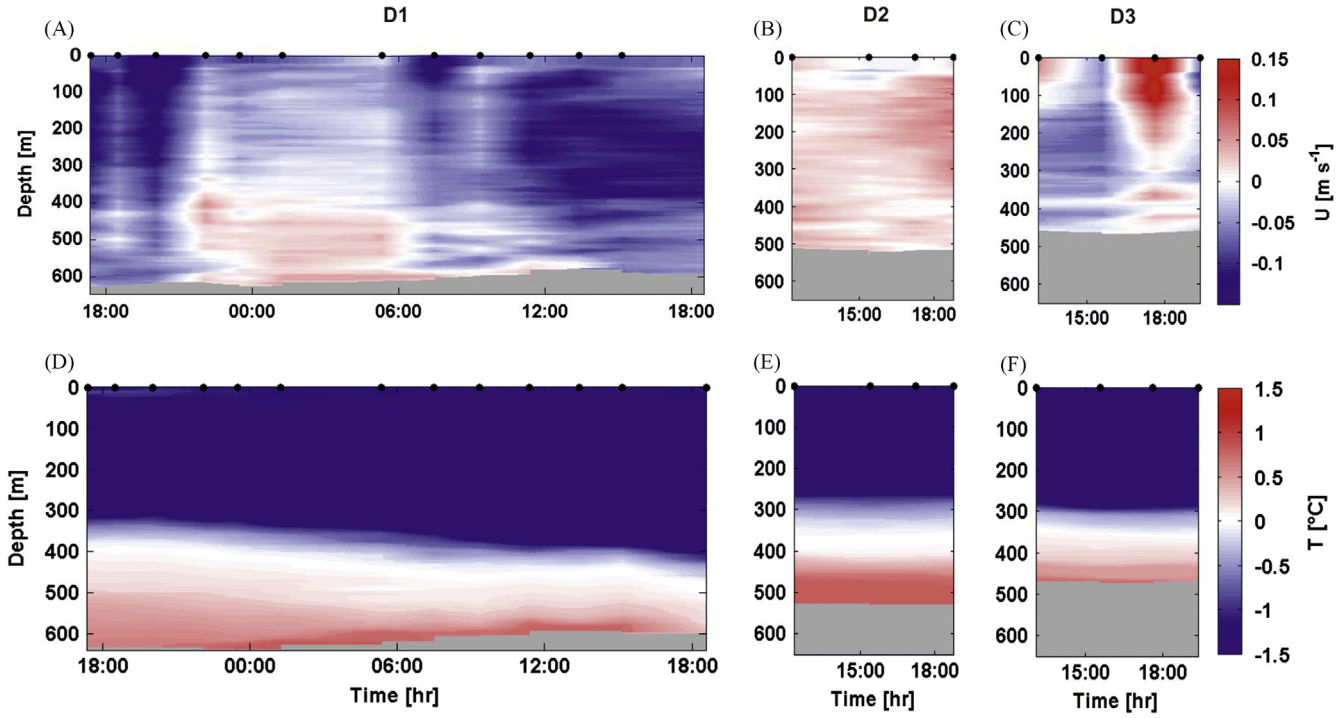

Fig. 11. Along-trough velocity (m s^{-1}, positive towards southeast) at the drift stations, mean positions given in Fig. 2. Observation times are given by the black circles (a) Station D1, starting date 18 Dec 2008 (b) Station D2, starting date 21 Dec 2008 (c) Station D3, starting date 17 Dec 2008.

Inaccurate bathymetry presents a serious limitation to model studies and large areas of the Amundsen shelf are still uncharted despite strong efforts to remedy this over recent years. The trough is 150 m too shallow and its centerline is 20 km too far east in the model. The bathymetric survey performed by Araon in 2014 also shows that the sill depth of the trough leading from the eastern Getz basins to the central ones (Fig. 7) is in reality up to 200 m deeper than in the model. Since this is deeper than the sill depth between the Dotson trough and the shelf break it could have large consequences for the circulation on the shelf. Similar major errors are likely present also in the other uncharted areas of the western Amundsen Sea Shelf. Consequently a significant part of the discrepancy between model results and observations may be explained by errors and gaps in the model bathymetry.

Nonetheless, qualitative results have been obtained which pertain to both in-situ and model data. The on-shore oceanic heat flux on the central Amundsen Sea shelf appears to be caused mainly by barotropic currents circulating in a clockwise direction in the Dotson trough. The barotropic currents move warm water on-shore at the eastern flank of the trough, and colder and fresher water off-shore at the western flank. Although this general circulation path was suggested by Ha et al. (2014), it has not previously been shown that it is the barotropic component of the current that is likely responsible for the major part of the heat flux. The results were inferred from calculations using mooring data (Figs. 5 and 6), cross-trough sections (Fig. 4), the drift stations (Fig. 11) and output from a regional set up of the MITgcm (Figs. 3, 5 and 6; Assmann et al., 2013). The findings imply that the main oceanic heat flux towards the glaciers is not driven by buoyancy forces arising as relatively dense water is lifted across the shelf break. This is in contrast to results in Arneborg et al. (2012), where the velocity structure (based on the first 10 months of the present mooring data set) was inferred to consist of a barotropic, fluctuating part that did not cause any net heat flux toward the coast and a baroclinic, steady current that gave rise to the main heat flux. Upward lifting of dense warm water induced by upwelling from westerly winds has been observed along the Amundsen Sea shelf break (Wåhlin et al., 2012), and it was proposed that such lifting over the shelf break and associated buoyancy-driven flow towards the glaciers is the main mechanism of oceanic heat transport towards the floating glaciers. Pritchard et al. (2012) concluded that the observed increased basal melt rates of West Antarctic ice shelves may be attributed to increased westerly winds (Young et al., 2011) thus implying the importance of a baroclinic buoyancy driven flow.

Apart from a regional scale influence, the wind can also cause localized phenomena, as shown in Wåhlin et al. (2015). Strong barotropic oscillations with a period of 2.5 days, identified as resonant topographic Rossby waves, were found at the outflow mooring S2. The oscillations dominate the local hydrography at most times and may exist due to the steep and shallow topography of the western slope. This again emphasizes the importance of reliable bathymetry data, as well as to use caution when relying only on sparse snap-shot data.

Further east on the continental shelf on the West Antarctic Peninsula, in a model study Dinniman et al. (2011) connected the warm water intrusions on the shelf with wind forcing, citing momentum advection of the increased flow along the slope as a possible mechanism for the inflow events. In contrast, the present results indicate that it is the strength of the horizontal circulation pattern on the continental shelf that modulates the heat transport. The variability of the barotropic velocity is correlated with local eastward winds on the shelf and shelf break area. This result was inferred by Wåhlin et al. (2013) using observations in the Dotson trough and also in the western inlet of the eastern Amundsen shelf channel by Assmann et al. (2013) employing model data. Both studies also suggest that it may be the velocity rather than the temperature of the inflowing deep water that is the major component of the heat flux onto the shelf. In conclusion, the wind may be the most important driver of the barotropic horizontal circulation path, which in turn is probably responsible for bringing the majority of the oceanic heat to the floating ice shelves in the

Dotson trough. To expand the knowledge about the shelf circulation, further long term observations as well as increased accuracy of the bathymetry data would be of great value.

Acknowledgments.

This work was supported by K-Polar Program (PP13020) of KOPRI and the Swedish Research Council (SRC). The authors would like to thank Sudipta Goswami and Paul Holland at British Antarctic Survey for performing the simulations with daily output. We are grateful to two anonymous reviewers for helpful and knowledgeable reviews that improved the paper. Ben Webber at University of East Anglia is thanked for fruitful discussions on the manuscript. We are deeply indebted to the captains and crews of the IBRVs Araon and Oden for professional support during the Amundsen expeditions.

H. K. Ha was supported by Inha University Research Grant (INHA-51416)."

References

Antonov, J.I., Seidov, D., Boyer, T.P., Locarnini, R.A., Mishonov, A.V., Garcia, H.E., Baranova, O.K., Zweng, M.M., Johnson, D.R., 2010. World Ocean Atlas 2009. In: Levitus, S. (Ed.), Volume 2. U.S. Gov. Print. Off., Washington, D. C, p. 184.

Arakawa, A., Lamb, V., 1977. Computational design of the basic dynamical processes of the UCLA general circulation model. Methods Comput. Phys. 17, 174–267.

Arneborg, L., Wåhlin, A.K., Björk, G., Liljebladh, B., Orsi, A.H., 2012. Persistent inflow of warm water onto the central Amundsen shelf. Nat. Geosci. 5 (12), 876–880.

Assmann, K.M., Jenkins, A., Shoosmith, D.R., Walker, D.P., Jacobs, S.S., Nicholls, K.W., 2013. Variability of circumpolar deep water transport onto the Amundsen sea continental shelf through a shelf break trough. J. Geophys. Res. Oceans 118, 6603–6620.

Chavanne, C.P., Heywood, K., Nicholls, K.W., Fer, I., 2010. Observations of the Antarctic slope undercurrent in the southeastern weddell sea. Geophys. Res. Lett. 37, 13.

Davis, R.E., 1976. Predictability of sea surface temperature and sea level pressure anomalies over the North Pacific Ocean. J. Phys. Oceanogr. 6, 249–266.

Dinniman, M., Klinck, J., Smith, W., 2011. A model study of circumpolar deep water on the West Antarctic Peninsula and ross sea continental shelves. Deep Sea ResII 58, 1508–1523.

Ha, H.K., Wåhlin, A.K., Kim, T.W., Lee, S.H., Lee, J.H., Lee, H.J., Hong, C.S., Arneborg, L., Björk, G., Kalén, O., 2014. Circulation and modification of warm deep water on the Central Amundsen shelf. J. Phys. Oceanogr. 44, 1493–1501.

Herraiz-Borreguero, L., Coleman, R., Allison, I., Rintoul, S.R., Craven, M., Williams, G.D., 2015. Circulation of modified circumpolar deep water and basal melt beneath the amery ice shelf, East Antarctica. J. Geophys. Res. Oceans 120 (4), http://dx.doi.org/10.1002/2015JC010697.

Holland, P.R.,N.Bruneau, Enright, C., Losch, M., Kurtz, N.T., Kwok, R., 2014. Modeled trends in Antarctic sea ice thickness. J. Clim. 27 (10), 3784–3801.

Jacobs, S.S., Jenkins, A., Giulivi, C., Detrieux, P., 2011. Stronger ocean circulation and increased melting under pine island glacier ice shelf. Nat. Geosci. 4, 519–523.

Jacobs, S.S., Giulivi, C., Dutrieux, P., Rignot, E., Nitsche, F., Mouginot, J., 2013. Getz ice shelf melting response to changes in ocean forcing. J. Geophys. Res. Oceans 118, 4152–4168.

Klinck, J.M., Hofmann, E.E., Beardsley, R.C., Salihoglu, B., Howard, S., 2004. Water-mass properties and circulation on the west antarctic peninsula continental shelf in Austral fall and winter 2001. Deep-Sea Res. II 51, 1925–1946.

Locarnini, R.A., Mishonov, A.V., Antonov, J.I., Boyer, T.P., Garcia, H.E., Baranova, O.K., Zweng, M.M., Johnson, D.R., 2010. World Ocean Atlas 2009. In: Levitus, S. (Ed.), Volume 1. U.S. Gov. Print. Off., Washington, D. C, p. 184.

Losch, M., 2008. Modelling ice shelf cavities in a z-coordinate ocean general circulation model. J. Geophys. Res. 113, C08043.

Losch, M., Menemenlis, D., Campin, J.-M., Heimbach, P., Hill, C., 2010. On the formulation of sea ice models. Part1: effects of different solver implications and parameterizations. Ocean Modell 33 (1–2), 129–144.

Marshall, J., Adcroft, A., Hill, C., Perelman, L., Heisey, C., 1997. A finite-volume, incompressible Navier Stokes model for studies of the ocean on parallel computers. J. Geograph. Res. 102 (C3), 5753–5766.

Moffat, C., Owens, B., Beardsley, R.C., 2009. On the characteristics of circumpolar deep water intrusions to the west Antarctic Peninsula continental shelf. J. Geophys. Res. 114, C05017.

Nakayama, Y., Schröder, M., Hellmer, H.H., 2013. From circumpolar deep water to the glacial melt water plume on the Eastern Amundsen shelf. Deep Sea Res. l 77, 50–62.

Padman, L., Fricker, H.A., Coleman, R., Howard, S., Erofeeva, S., 2002. A new tidal model for the Antarctic ice shelves and seas. Ann. Glaciol. 34, 247–254.

Paolo, F.S., Fricker, H.A., Padman, L., 2015. Volume loss from Antarctic ice shelves is accelerating. Science 348 (6232), 17.

Pawlowicz, R., Beardsley, B., Lentz, S., 2002. Classical tidal harmonic analysis including error estimates in MATLAB using T_TIDE. Comput. Geosci. 28, 929–937.

Pritchard, H.D, Ligtenberg, S.R.M., Fricker, H.A., Vaughan, D.G., van den Broeke, M.R., Padman, L., 2012. Antarctic ice-sheet loss driven by basal melting of ice shelves. Nature 484, 502–505.

Rignot, E., Mouginot, J., Morlighem, M., Seroussi, H., Scheuchl, B., 2014. Widespread, rapid grounding line retreat of pine island, Thwaites, Smith, and Kohler glaciers, West Antarctica, from 1992 to 2011. Geophys. Res. Lett. 41, 3502–3509.

Saha, S., et al., 2010. The NCEP climate forecast system reanalysis. Bull. Am. Meteorol. Soc. 91, 1015–1057.

Schodlok, M., Menemenlis, D., Rignot, E., Studinger, M., 2012. Sensitivity of the ice-shelf/ocean system to the sub-ice-shelf cavity shape measured by NASA icebridge in pine Island Glacier, West Antarctica. Ann. Glaciol. 53, 156–162.

St. Laurent, P., Klinck, J., Dinniman, M., 2013. On the role of coastal troughs in the circulation of warm circumpolar deep water on Antarctic shelves. J. Phys. Oceanogr. 43, 51–64.

Thoma, M., Jenkins, A., Holland, D., Jacobs, S., 2008. Modelling circumpolar deep water intrusions on the Amundsen sea continental shelf, Antarctica. Geophys. Res. Lett. 35, L18602.

Thompson, A.F., Heywood, K.J., Schmidtko, S., Stewart, A.L., 2014. Observational evidence of an eddy overturning at the Antarctic margins. Nat. Geosci. 7, 879–884.

Timmermann, R., Le Brocq, A., Deen, T., Domack, E., Dutrieux, P., Galton-Fenzi, B., Hellmer, H., Humbert, A., Jansen, D., Jenkins, A., Lambrecht, A., Makinson, K., Niederjasper, F., Nitsche, F., Nøst, O.A., Smedsrud, L.H., Smith, W.H.F., 2010. A consistent data set of Antarctic ice sheet topography, cavity geometry, and global bathymetry. Earth Syst. Sci. Data 2 (2), 261–273.

Wåhlin, A.K., Yuan, X., Björk, G., Nohr, C., 2010. Inflow of warm circumpolar deep water in the central Amundsen shelf. J. Phys. Oceanogr. 40 (6), 1427–1434.

Wåhlin, A.K., Muench, R.D., Arneborg, L., Björk, G., Ha, H.K., Lee, S.H., Alsén, H., 2012. Some implications of Ekman layer dynamics for cross-shelf exchange in the Amundsen sea. J. Phys. Oceanogr. 42, 1461–1474.

Wåhlin, A., Kalén, O., Arneborg, L., Björk, G., Carvajal, G., Ha, H.K., Kim, T.W., Lee, S.H., Lee, J.H., Stranne, C., 2013. Variability of warm deep water inflow in a submarine trough on the amundsen sea shelf. J. Phys. Oceanogr. 43, 2054–2070.

Wåhlin, A., Kalén, O., Assmann, K.M., Darelius, E., Ha, H.K., Kim, T.W., Lee, S.H., 2015. Sub-inertial oscillations on the Amundsen sea shelf, Antarctica. J. Phys. Oceanogr., accepted.

Walker, D.P., Brandon, M.A., Jenkins, A., Allen, J.T., Dowdeswell, J.A., Evans, J., 2007. Oceanic heat transport onto the Amundsen sea shelf through a submarine glacial trough. Geophys. Res. Lett. 34, L02602.

Walker, D.P., Jenkins, A., Assmann, K.M., Shoosmith, D.R., Brandon, M.A., 2013. Oceanographic observations at the shelf break of the Amundsen sea, Antarctica. J. Geophys. Res.: Oceans 118 (6), 2906–2918.

Young, I.R., Zieger, S., Babanin, A.V., 2011. Global trends in wind speed and wave height. Science 332 (6028), 451–455.